Science Advances

AAAS

Supplementary Materials for

Quasi–solid state rechargeable Na-CO₂ batteries with reduced graphene oxide Na anodes

Xiaofei Hu, Zifan Li, Yaran Zhao, Jianchao Sun, Qing Zhao, Jianbin Wang, Zhanliang Tao, Jun Chen

The PDF file includes:

Other Supplementary Material for this manuscript includes the following:
(available at advances.sciencemag.org/cgi/content/full/3/2/e1602396/DC1)

Chemicals and materials

Poly(vinylidene fluoride-co-hexafluoropropylene) (PVdF-HFP) with an average molecular weight of 455,000 and fumed silica are purchased from Sigma-Aldrich. Tetraethylene glycol dimethyl ether (TEGDME) (Aladdin) solvent is stilled by reduced pressure distillation and stored with activated 4 Å molecular sieves (beads 8-12mesh, J&k) in glove box (H_2O and O_2 < 1 ppm). Prior to use, $NaClO_4$ (anhydrous, Alfa Aesar) are dried under vacuum at 120°C for 10 hours. Multi-wall carbon nanotubes (CNTs) are bought from Cnano Technology Ltd. Fullerene C_{60} is from Strem. Reduced graphene oxide (rGO) is prepared by combining a modified Hummer's method and a reduction process with hydrazine hydrate. Silver nanowires are purchased from Beijing Coupling Technology Ltd. Notably, the original silver nanowires (stored in glycerin) need to be rinsed with ethanol and dried under vacuum at 25°C overnight prior to use.

Fabrication of curly carbon nanosheets

The curly carbon nanosheets were synthesized by direct chemical reaction of $2Mg + CO_2 \rightarrow C + 2MgO$. In the reaction, a high-purity Al_2O_3 boat ($20 \times 20 \times 90$ mm^3) loaded with polished Mg sheets ($10 \times 2 \times 60$ mm^3) was put into a horizontal tube furnace. The furnace was heated to 800 °C for 2 h with CO_2 flow. After cooling to room temperature, the black powder was stirred in 10 wt% HCl aqueous solution at 25 °C for 1.5 h. The sample was filtered, washed by distilled water and absolute ethyl alcohol, dried at 100 °C in vacuum for 10 h to obtain curly carbon nanosheets.

Material characterization

X-ray diffraction patterns of cathodes are collected from a Rigaku MiniFlex600 X-ray diffractometer with Cu K radiation (λ=1.54 Å). Scanning electron microscopic images are

taken by a field emission electron microscope (JEOL JSM-7500F) with acceleration voltage of 5 kV and work distance of 8 mm. Transmission electron microscopy and high-resolution transmission electron microscopy images are measured by a Philips Tecnai G2F-20 with acceleration voltage of 200 kV and equipped with electron energy loss spectroscopy. The Raman spectrum is recorded by Thermo-Fisher Scientific with excitation wavelength of 532 nm. Fourier transform infrared spectroscopy (FTIR) is collected on BRUKER TENSOR II. Thermal gravimetric analyzer (TGA) curves come from NETZSCH STA 449 F3 Jupiter.

Battery assembly

The quasi-solid-state Na–CO_2 batteries of this study are tested in CR2032 coin-type batteries and pouch-type batteries. Each coin-type battery consists of a sodium metal anode (10 mm in diameter and 1 mm in thickness), a cathode placed on a nickel mesh supporter (10 mm in diameter), a PVdF-HFP/SiO_2 composite film (16 mm in diameter and 75 μm in thickness) with loading of 1 mol L^{-1} NaTFSI/TEGDME electrolyte. The cathode case is drilled one hole (4 mm in diameter) for CO_2 diffusion. Then, the assembled batteries are placed in a glass vessel (200 mL) filled with high pure CO_2. It is worth noting that all the CO_2 atmosphere under battery test is at 1 atm unless special note. Before discharge/charge cycling, batteries rest for 5 h. Pouch-type Na–CO_2 batteries are made up of one plastic case (20×20 cm^2), a Na anode on Cu foil (18×18 cm^2, 3.0 g), a piece of CPE (22×22 cm^2), and a carbon cathode (20×20 cm^2). The total mass of this pouch-type batttery is ~10.0 g. Before operation at room temperature in pure CO_2, this battery is heated at 70°C to release innerstress for 3 h. During this process, in order to further intergrate all battery components tightly, one 304 stainless steel plate ($25 \times 25 \times 5$ cm^2) with 400 holes (5 mm in diameter) is put on this battery with a substrate of the other stainless steel plate ($25 \times 25 \times 2$ cm^2).

Electrochemical test

The data of galvanostatic discharge/charge operation are performed with LAND CT2001A battery test instruments. The capacity and current density are based on the mass of carbon nanotubes with loading of 0.3 mg cm^{-2}. Cyclic voltammograms are carried out through a Parstat 2273 electrochemical workstation within the potential window of 1.4–4.0 V (vs. Na/Na$^+$). Electrochemical impedance spectroscopy is tested on Parstat 263A potentiostat/galvanostat workstation (AMETEK Company) in the frequency range of 0.1–10^5 Hz. The pouch-type batteries operate in battery-test box equipped with a pressure meter. Cyclic voltammograms of deposition and precipitation are collected on a Parstat 4000 electrochemical workstation with sweep speed of 0.5 V s^{-1} between −1.0~3.0 V (vs. Na/Na$^+$).

CO$_2$ evolution test

In brief, the batteries with pre-filled mixture of Na$_2$CO$_3$ and carbon nanotubes or just with pure Na$_2$CO$_3$ are charged at 200 mA g^{-1}. The theoretical value of CO$_2$-evolution rate is based on the reaction of $3CO_2 + 4Na \leftrightarrow 2Na_2CO_3 + C$ is 1.17 p.p.m. min^{-1}. CO$_2$-evolution is examined by SKY2000-CO$_2$ (Shenzhen, China), in which the sensor is NDIR SENSOR MSH-PS/CO$_2$ (Derbyshire, United Kingdom). The measuring range is 0–500 ppm with response time of < 15 s. Dynament infrared sensors are operated by NDIR principle to test the presence of the target gas (CO$_2$).

Energy density calculation

We have confirmed the discharge/charge reaction of Na–CO$_2$ battery

$$4Na + 3CO_2 \leftrightarrow 2NaCO_3 + C, E = 2.35 \text{ V} \qquad (1)$$
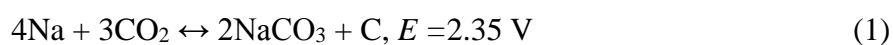
Where E is the open circuit voltage under standard conditions (0°C, 1.0 atm). The energy density (W) of pouch-type battery can be calculated by equation (2)

$$W = C \times V / \left(\frac{C}{C_c} + \mathrm{m}_c \right)$$

(2)

where C (1100 mAh) is the capacity of full discharged cathode; C_c (479 mAh g^{-1}) is the

theoretical capacity of Na–CO$_2$ battery based on all discharge products. V (2.13 V) is the

discharge voltage. m_c (1.0 g) is the mass of carbon material on cathode. The energy density is

1022 Wh·kg^{-1} based on carbon material and discharge products. In consideration of the total

mass of whole pouch-type battery, the energy density is 232 Wh·kg^{-1} based on the equation of

$W = C \times V/M$, where M (10.0 g) is the mass of whole battery.

Density function theory (DFT) calculation

The DFT calculations were performed by Vienna ab Initio Simulation Package (VASP) (*31*).

The projector augmented wave (PAW) method (*32*) and generalized gradient approximation

(GGA) with the function of Perdew−Burke−Ernzerhof (PBE) (*33*) were employed. The

cut-off energy for plane-wave basis was set to 600 eV. The total energy and the residual

Hellmann−Feynman force were converged to 10-5 eV/atom and 0.02eV/Å, respectively. All

the geometry relaxations were performed using a 5 × 5 × 5 k-point mesh. The MCNTs (5, 5)

was chosen as the model to simulate the CO$_2$ adsorption. We considered both the

perpendicular and parallel adsorption direction and different adsorption configurations (top,

hollow and bridge), the results are illustrated in fig. S9

$$Eads = E (CO_2\text{-MCNTs}) − E (MCNTs) − E (CO_2)$$

E (CO$_2$-MCNTs), E (MCNTs), and E (CO$_2$) represent the energy of CO$_2$ adsorbed on MCNTs,

a-MCNTs and CO$_2$, respectively. The negative value of Eads means the configuration is

thermodynamically stable. The more negative value of Eads corresponds to the more

stable configuration.

Explanatory calculation

According to the reaction of $4Na + 3CO_2 \leftrightarrow 2Na_2CO_3 + C$, 2.25 kg CO_2 (released by a liter of gasoline) could theoretically produce 4.30 kWh electric energy, which is about half of the equivalent energy of a liter of gasoline. If the released CO_2 are all conversed in Na-CO_2 batteries and the energy efficiency of electromotor (~80%)/gasoline engine (25%) are considered, the driven miles of hybrid electric vehicles would be doubled or tripled.
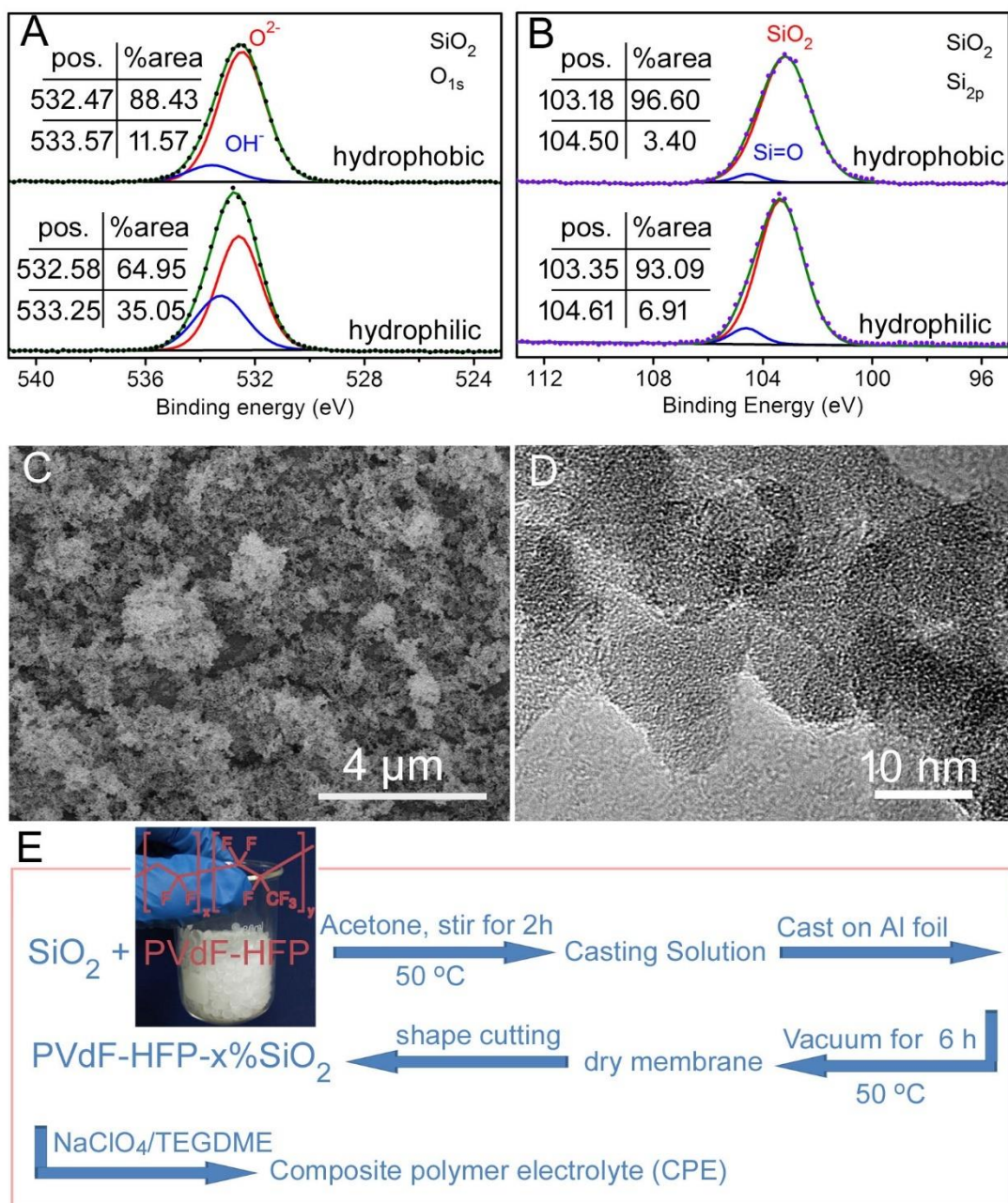
fig. S1. The raw materials and synthesis procedures of CPE. X-ray photoelectron spectroscopy (XPS) of hydrophobic SiO_2 and hydrophilic SiO_2, (**A**) O1s, (**B**) Si2p. (**C, D**) Commercial fumed silica in hydrophobic type. (**E**) The preparation procedures of CPE. The iset photograph shows commercial PVdF-HFP particles.

Hydrophilic and hydrophobic fumed silica (SiO_2) could be comercially obtained. The former one possesses more superfacial silicone hydroxyl at 533.25~533.57 eV than the later one (fig. S1A). A higher ratio of the signals SiO_2 (~104 eV)/SiO_2 (~103 eV) is observed for samples responsible for the higher level of wettability (*34*) (fig. S1B). Finally, we choose

hydrophobic SiO$_2$ as fillers into CPE. Hydrophobic SiO$_2$ particles (7~10 nm) are slightly agglomerated   (fig. S1C and D). Commercial PVdF-HFP is white particles with dimaters of 4~5 mm. After multi-step preparation, a transparent membrane is obtained.
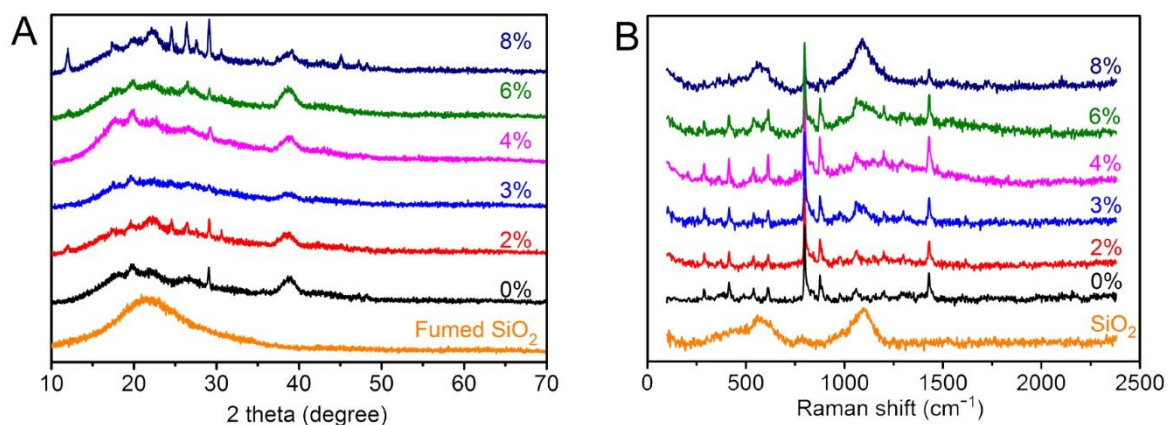
fig. S2. The optimization of Na$^+$-CPE. (**A**) XRD patterns and (**B**) Raman of polymer matrix of CPE with different percentage compositions of fumed silica.

The added nano ceramic filler promotes amorphicity of CPE by strongly interacting with polymer host (*18*). The amorphous region benefits ionic transfer. Therefore, the ceramic filler of nanosized SiO$_2$ in CPE is a critical factor for ionic conductivity.
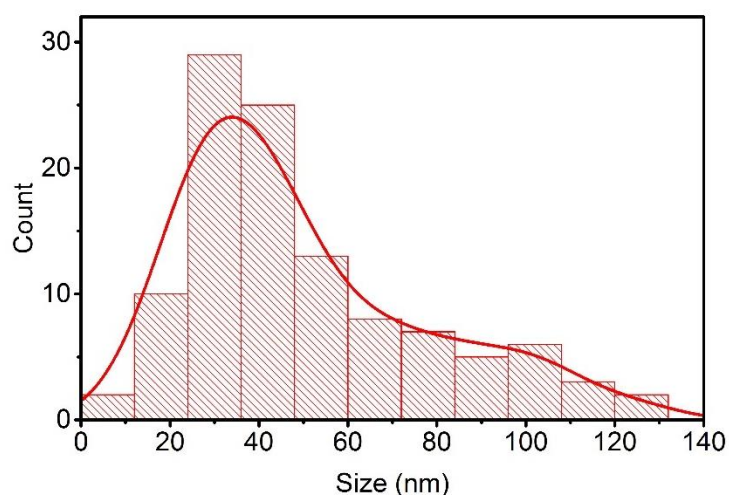
fig. S3. The pore size distribution of CPE. The sampling number is 100. The centered pore size is ~30 nm.
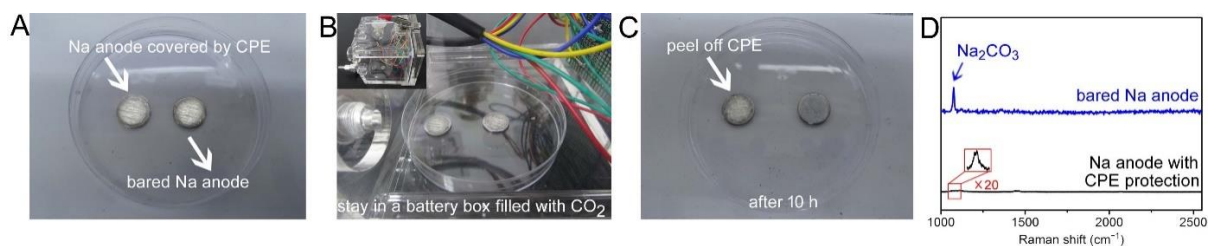
**fig. S4. The CO₂ diffusion test.** (**A**) Two Na anodes with or without CPE protection. (**B**) Two anodes stay in a battery box filled with CO_2. The inset graph is the full view of the battery box. (**C**) After 10 h, the bared Na anode becomes gloomy; while the anode with CPE protection is relatively bright. (**D**) Raman of two Na anodes after staying in CO_2 for 10 h. We observe strong signal of Na_2CO_3 on the bared Na anode. In contrast, signal of Na_2CO_3 on the CPE-protected Na anode is weak. These results indicate that the CPE could suppress CO_2 diffusion onto the anode of Na-CO_2 batteries.
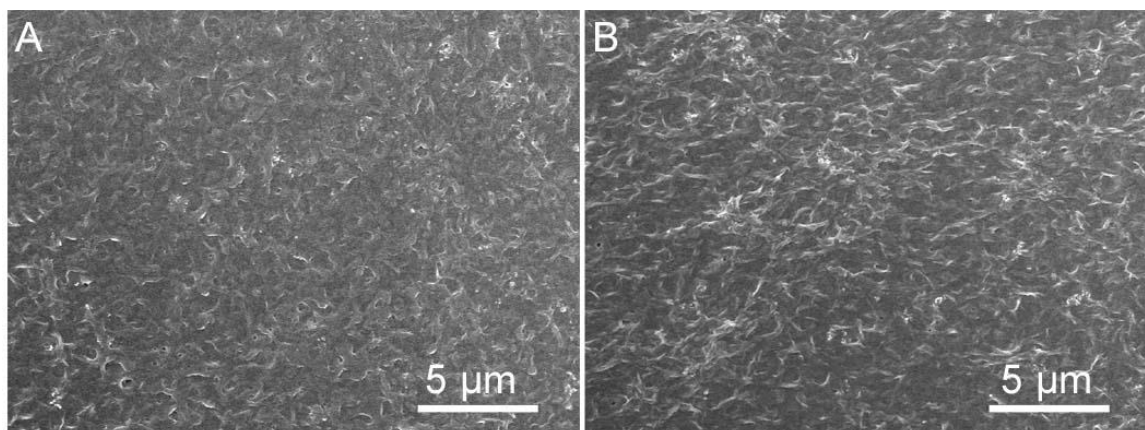
fig. S5. SEM images of CPE surface. (**A**) Front side next to air and (**B**) opposite side next to Al foil.
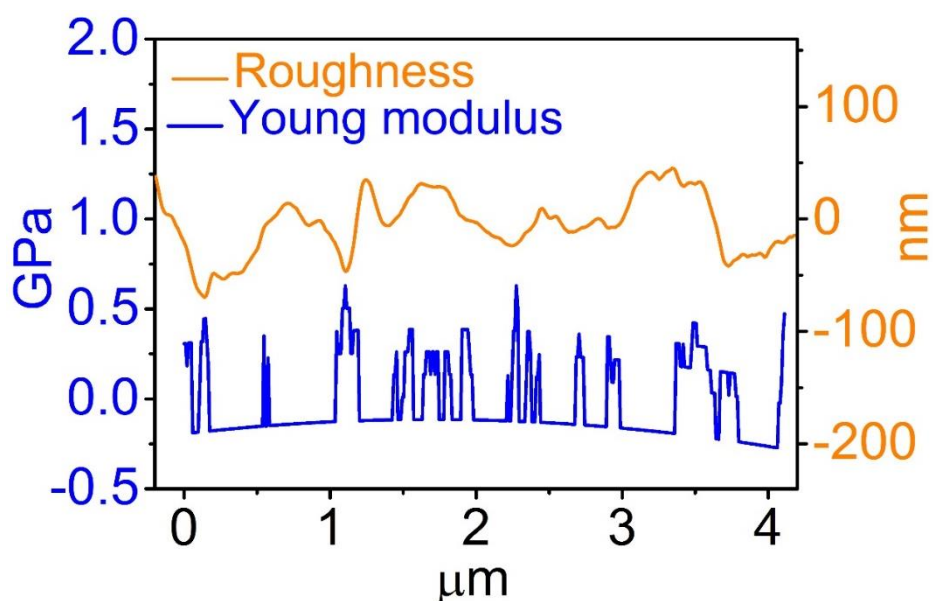
fig. S6. Roughness and Young modulus of polymer matrix (PVDF-HFP/4% SiO₂) of CPE.
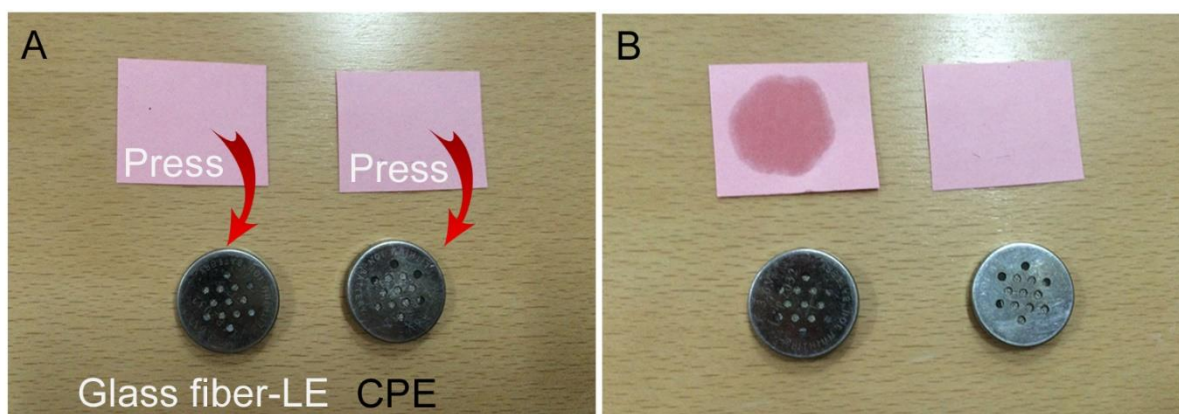
fig. S7. Leakage test of Na-CO₂ batteries. LE is 1 M NaClO₄/TEGDME solution. LE-based battery and CPE-based battery (**A**) before and (**B**) after pressing by a piece of dry paper.

The Na-CO₂ battery with CPE successfully suppresses leakage in comparison with the battery that contains glass fiber-LE. After pressing tightly on a piece of paper, CPE based battery does not make the paper wet but LE-based battery makes the paper wet. Both CPE and glass fiber in batteries are 16 mm in diameter.
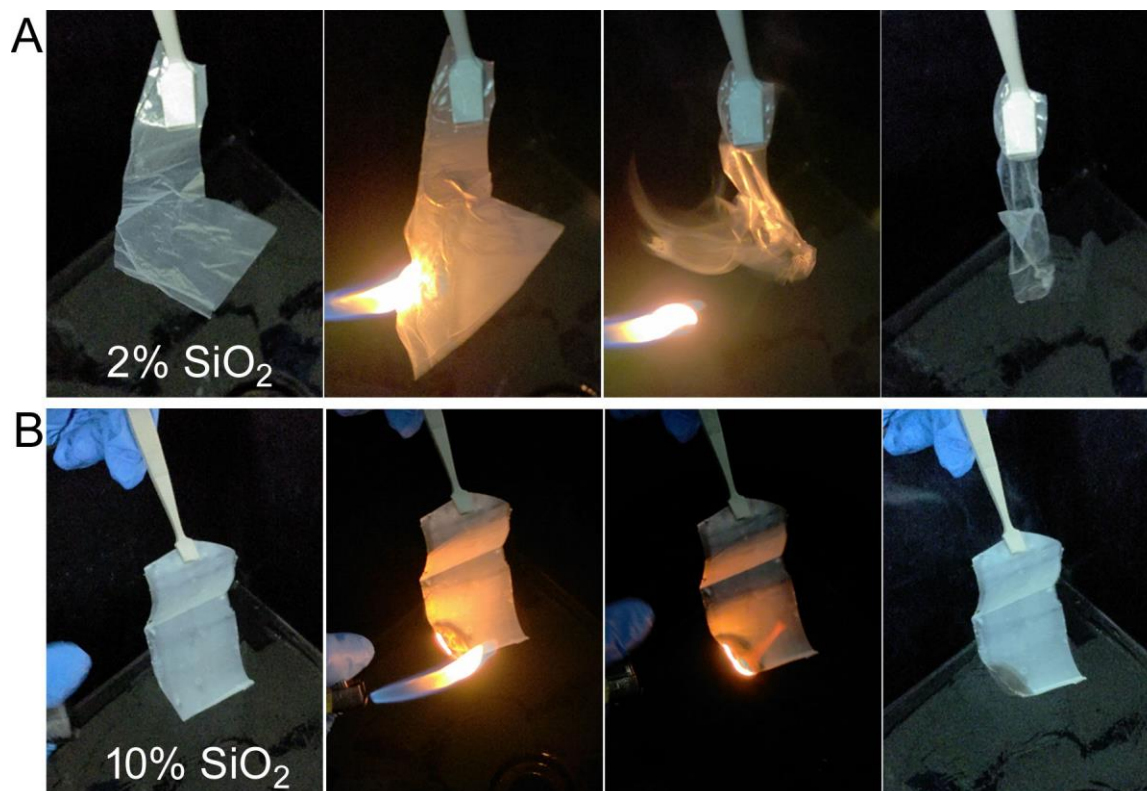
fig. S8. Inflammability test of polymer matrix (PVDF-HFP/SiO₂) of CPE. Inflammability test of polymer matrix (PVdF-HFP/SiO$_2$) of CPE with (**A**) 2% SiO$_2$, (**B**) 10% SiO$_2$. The fire from a lighter is ~500°C.
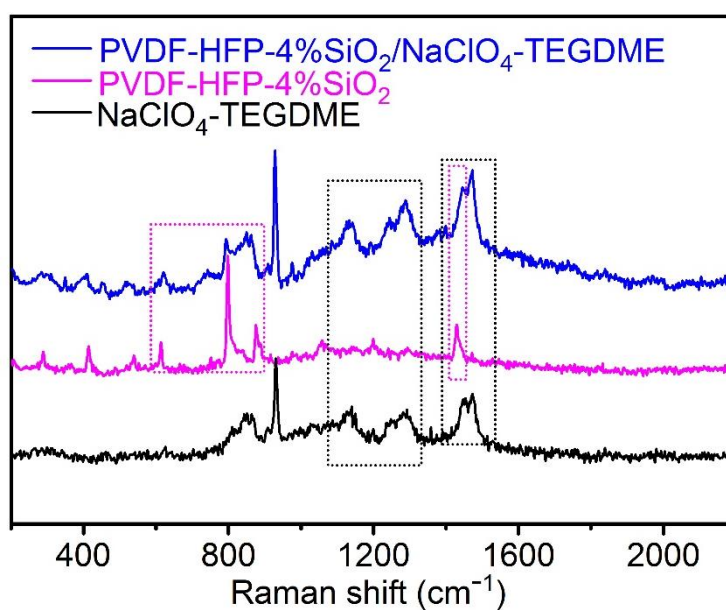
fig. S9. Raman of CPE, polymer matrix, and liquid electrolyte.

fig. S10. Transporting mechanism of Na⁺ in polymer chains and work window of CPE.
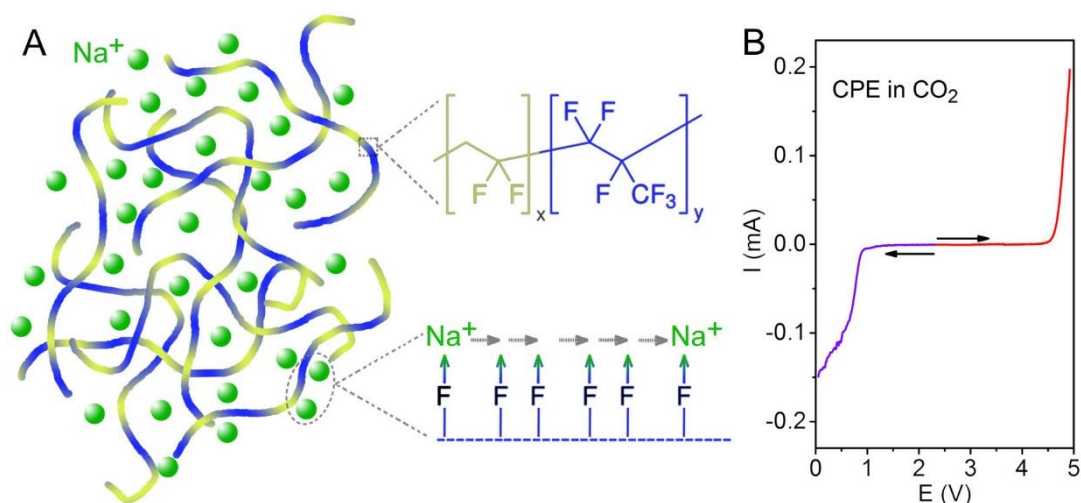(**A**) A schematic diagram of Na^+ transportation in polymer chains of CPE. (**B**) Linear sweep voltammetry (LSV) curves of CPE in CO_2.

By absorbing 1 M NaClO₄/TEGDME (liquid electrolyte) into polymer matrix of PVdF-HFP-4%SiO₂, the finally obtained CPE is enabled with 30 wt% liquid electrolyte and 70% polymer matrix. The ionic diffusion of solvated Na^+ in liquid electrolyte undoubtedly makes a contribution to Na^+-conductivity of CPE. In addition, it is reported that there is interaction between Li^+ and F atoms in PVdF-HFP based CPE (*35,36*). Since Li^+ and Na^+ have similar physical and chemical properties, the Na^+-transfer in PVdF-HFP probably cannot live without F atoms on macromolecular chains of PVdF-HFP. Therefore, the large amount of F atoms and TEGDME agent would play a key role in the Na^+-diffusion in CPE.
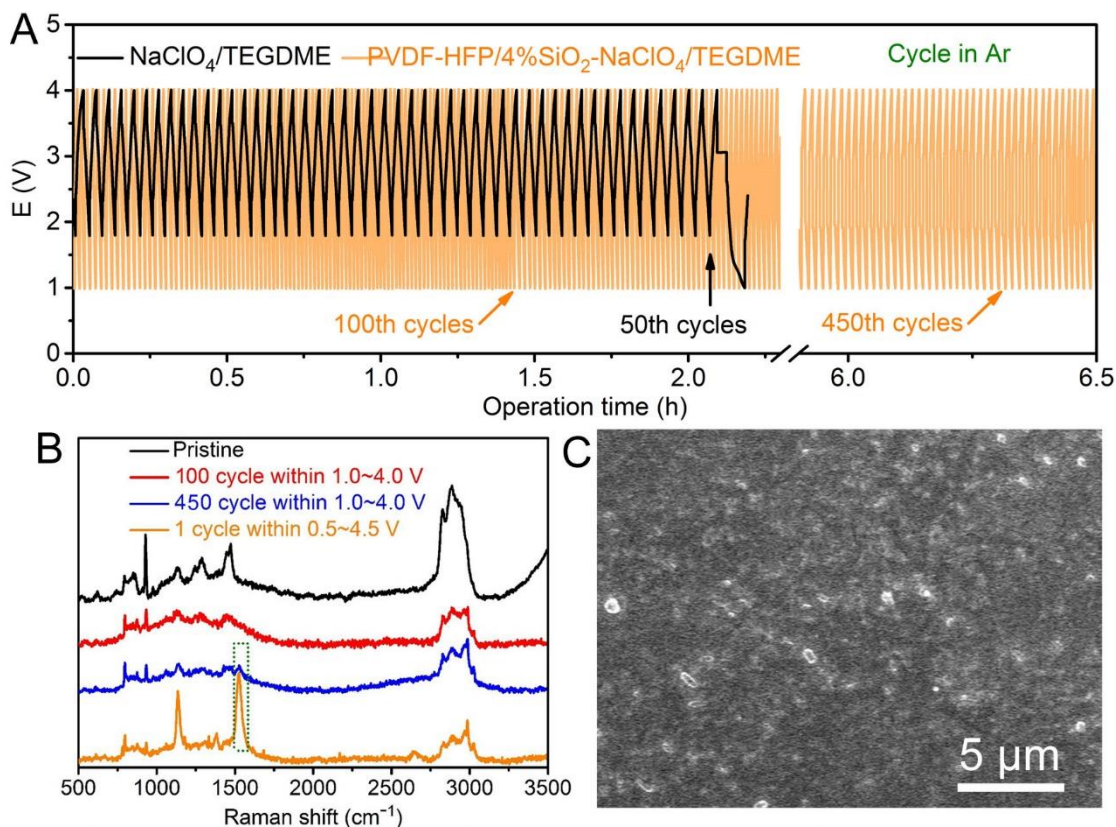
**fig. S11. Long-term stability analysis of CPE.** (**A**) Long-term stability comparision of CPE and LE in Na-CO$_2$ batteries in Ar at 0.3 mA cm^{-2}. (**B**) Raman spectrum of CPE in different states. (**C**) SEM image of CPE surface after 100 cycles.

The essential factors of a long-term stable battery system generally include two major aspects, namely the electrochemical stability of electrolytes and uniform Na$^+$-plating/stripping on anode under continuous discharge/charge currents. Obviously, CPE could endure voltage range of 1.0~4.0 V for hundreds of cycles in Ar (fig. S11A), in which the electric double layer capacitance behavior indicates no side reactions involving CPE decomposition. On the contrast, LE could support battery operation between 1.8~4.0 V for many cycles in Ar, but it reveals an obvious capacity once its voltage window extends to 1.0~4.0 V. This capacity obtained in Ar responds to LE decomposition, which is confirmed by Raman spectrum (fig. S11B). In detail, Raman peaks of CPE after 100 cycles are similar to that of the pristine state. While, there emerges a new peak which is clearly seen after the operation window extending to 0.5~4.5 V, which should belong to by-products from LE decomposition. The

surface of CPE after 100 cycles still remains nondestructive and more smooth (fig. S11C) in comparision with its initial state in fig. S5.

It is worth noting that NaClO$_4$/TEGDME solution would be decomposed within voltage of 1.0~1.8 V when absorbed in glass fiber; While, it keeps electrochemically stable within 1.0~4 V once integrated into CPE. The reason is that the polymer matrix of CPE accommodates the solution, avoiding too much exposure to electrodes and thus suppressing side reactions.
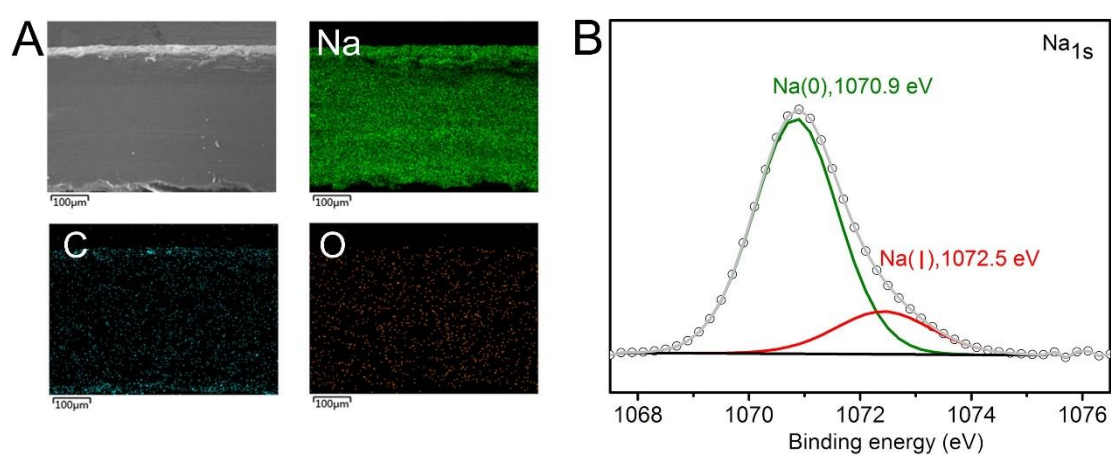
fig. S12. Element mapping and XPS-Na1s of rGO-Na anode. (**A**) Element mapping and (**B**) XPS-Na1s of rGO-Na anode.
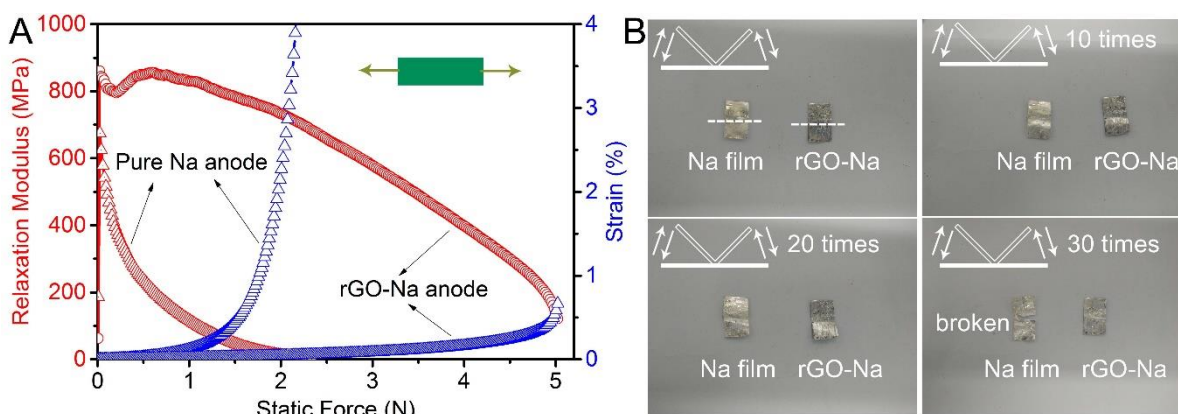
fig. S13. Mechanical strength and toughness of pure Na and rGO-Na anodes.

(**A**) Relaxation modulus and Strain tests of pure Na anode and rGO-Na anode. This test is carried out on DMA Q800. (**B**) Toughness test. We use two tweezers to bend the Na film and rGO-Na film.

The pristine size of belts (anode materials) in fig. S13A is 10.0 mm × 30.0 mm × 0.5 mm. The speed of static force is 0.5 N min^{-1}. As the static force increases, both pure Na and rGO-Na belts extend. The strain of pure Na belt is close to 4% when the static force is 2 N. While, the strain of rGO-Na belt is still < 0.7% when the static force is 5 N, indicating that rGO foam improves the mechanical strength of rGO-Na anode.

The pristine size of belts in fig. S13B is 10.0 mm × 15.0 mm × 0.5 mm. Both pure Na belt and rGO-Na belt are bended for dozens of times. The pure Na belt is broken after bending for 30 times; while, the rGO-Na belt is still intact, suggesting that rGO foam improves the toughness of rGO-Na anode.
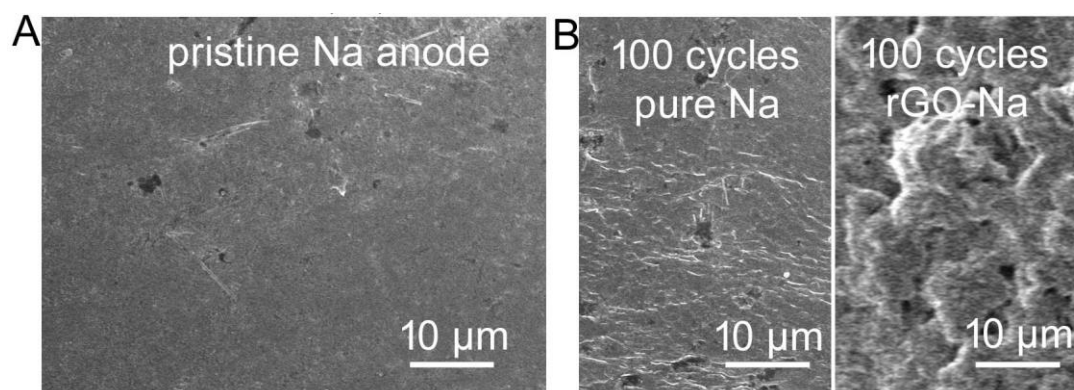
fig. S14. Anode analysis. (**A**) SEM image of pure Na anode. (**B**) SEM images of pure Na anode and rGO-Na anode surface after 100 cycles.
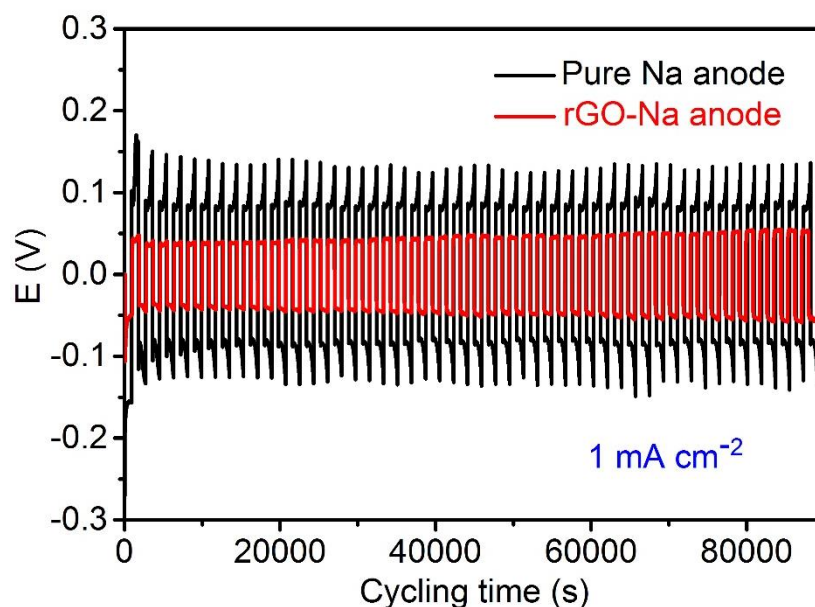
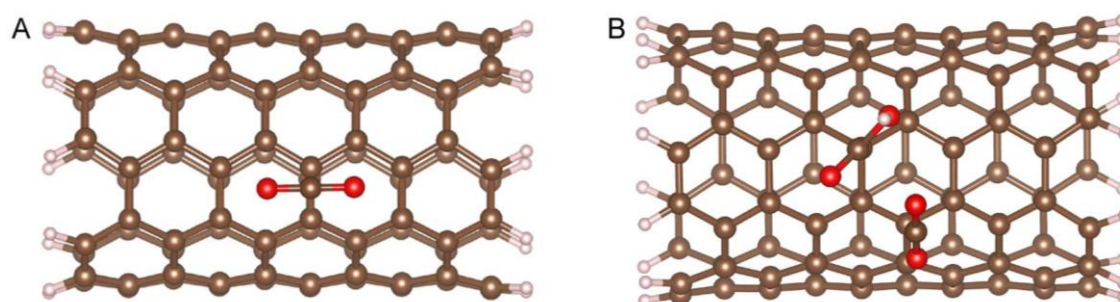**fig. S15. Galvanostatic cycling of a symmetric rGO-Na electrodes and pure Na anodes.**

fig. S16. The optimized geometries of CO₂ adsorbed on MCNT and a-MCNTs. The optimized geometries of CO_2 adsorbed on (**A**) MCNT and (**B**) a-MCNTs.

Density function theory (DFT) calculations were performed to get further insight into the interaction between CO_2 and the substrates. The CO_2 takes the parallel adsorption mode, in which the CO_2 above the C-C bond with the two O atoms locates on the hexgonal center of pristine MCNTs. The adsorption energy of CO_2 adsorbed on pristine MCNTs is 0.17 eV, suggesting a weak physical adsorption. In contrast, CO_2 takes the end-on adsorption mode with one of the O atom close to the -OH group of a-MCNTs, and the corresponding adsorption energy is 0.32 eV. The O-H...O bond length is about 3 Å, indicating the formation of hydrogen bond. The formation of hydrogen bond helps to increase the interaction between CO_2 and a-MCNTs, thus promoting the battery performance.
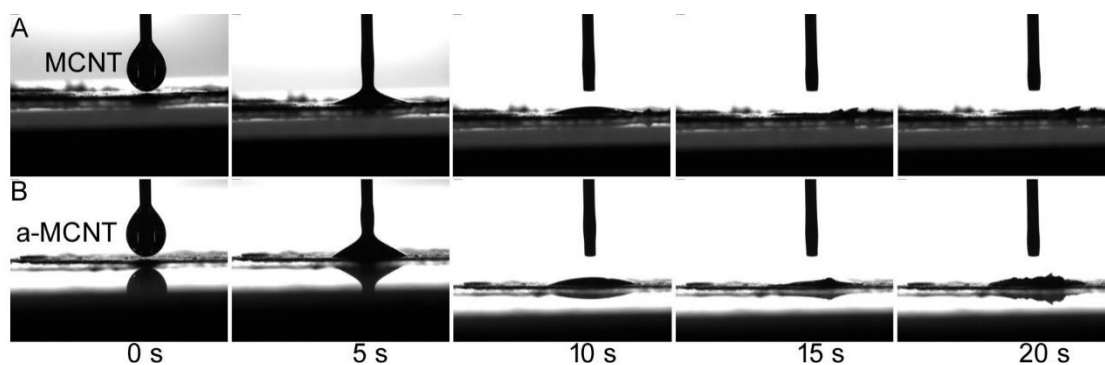
fig. S17. Soluble inflation of MCNTs and a-MCNTs toward TEGDME solvent. Soluble inflation of (**A**) MCNTs and (**B**) a-MCNTs towards TEGDME solvent.

The substrate surface tested here is not compacted tightly, so as to distinguish from contact angle test. In comparision with the pristine MCNTs, a-MCNTs obviously exhibit soluble inflation, indicating much better wettability towards TEGDME.

This boiling treatment makes TEGDME solvent into the internal walls of a-MCNTs and enables a-MCNTs with higher electronic conductivity, activated sp^2-type carbon surface as well as much better wettability towards TEGDME than pristine MCNTs. These properties would be beneficial to the cathode reaction of $4Na^+ + 3CO_2 + 4e^- \leftrightarrow 2Na_2CO_3 + C$ in the gas/CPE-LE/a-MCNTs surface/interface boundaries.
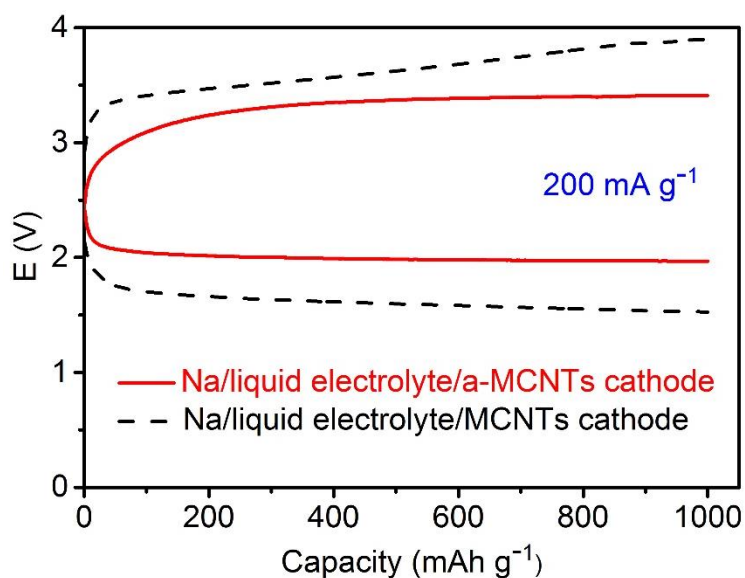
fig. S18. Initial discharge and charge profiles of Na-CO$_2$ batteries with the configuration of Na/NaClO$_4$-TEGDME/cathode.
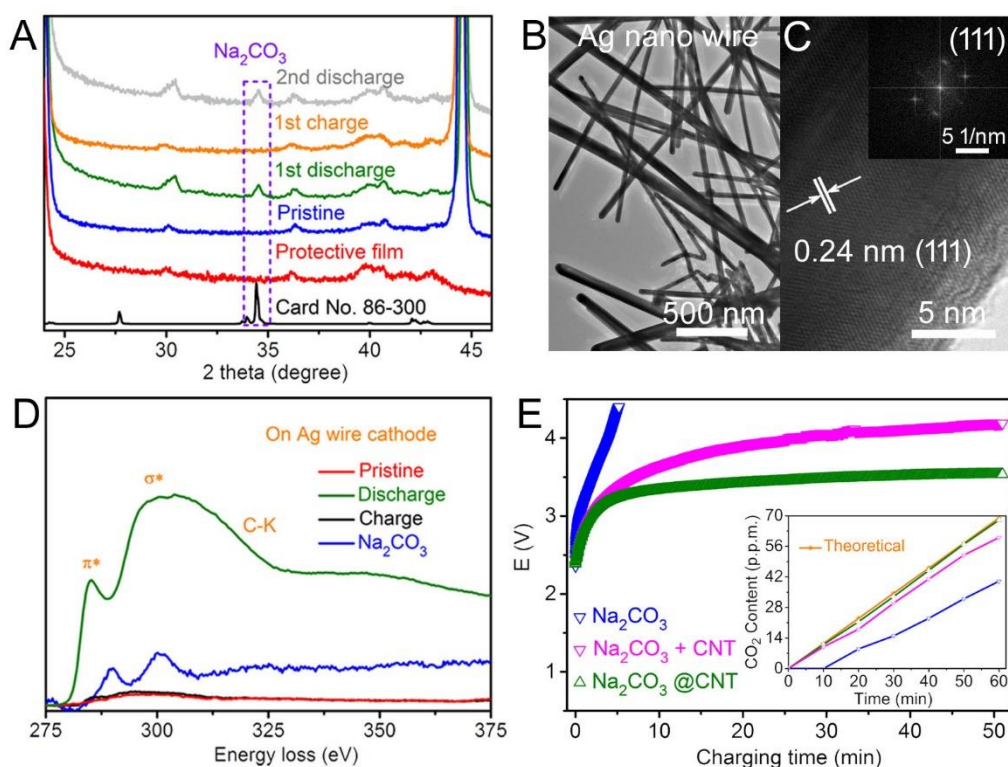
**fig. S19. Reaction mechanism analysis of Na-CO₂ batteries.** (**A**) XRD patterns of a-MCNTs cathodes in different states. (**B**, **C**) TEM images of Ag nanowire cathode for C examination. (**D**) EELS of Ag nanowire cathodes in different states. (**E**) Charge curves of Na-CO₂ batteries with pre-filled cathodes and the inset CO₂-evolution test.

XRD is applied to record the reaction progress of discharge and charge (fig. 19A). The peak of Na_2CO_3 initially appears and disappears after discharge and charge, respectively. This phenomenon indicates the reversible formation and decomposition of Na_2CO_3 above equation. We use an Ag nanowire cathode in the battery (figs. 19B,C) to confirm the existence of carbon in discharge products because of potential disturbance from a-MCNTs to the examination of carbon product. Signals of Ag nanowire cathode at different states are collected by electron energy loss spectroscopy (EELS). Compared with the pristine Ag nanowire cathode (red line in fig. S19D), we observe the peak with visible edges at 280.8 eV after the battery discharge at 200 mA g^{-1} for 1 h (green line in fig. S19D). This suggests the existence of sp^2 carbon atom (*18*), which comes from carbon substance rather than carbonate (blue line in fig. S19D). After charge, the peak of carbon disappears (black line in fig. S19D), indicating the reversibility of product carbon. In order to further verify whether Na_2CO_2 could react with C to release CO_2 on charging, we prepare various cathodes with re-filled Na_2CO_3

and a-MCNTs and examine the evolved gas on charging via a portable CO_2-analyzer. The theoretical value of CO_2-evolution is 1.17 p.p.m. min^{-1}. In comparision with pure bulk Na_2CO_3 and the physical mixture of bulk Na_2CO_3/a-MCNTs, the cathode with prefilled ball-milling Na_2CO_3/a-MCNTs hybrid shows the lowest charging voltage at ~3.5 V and its CO_2-evolution rate is the closest to above theoretical value (fig. S19E and its inset graph). This indicates the reactivity of Na_2CO_3/carbon and the importance of tightly contact towards the reactants.
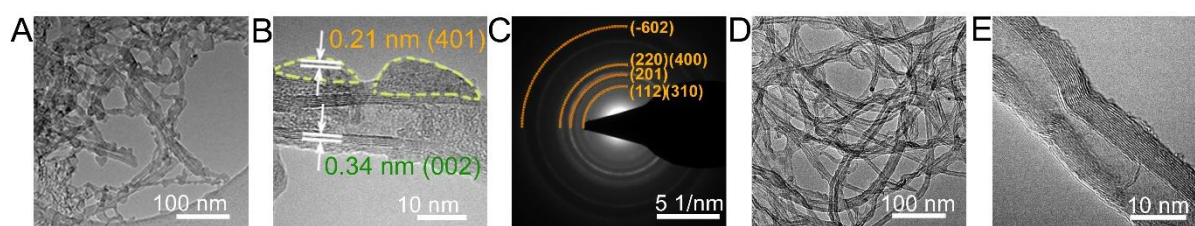

fig. S20. Discharge product analysis of quasi–solid state Na-CO₂ battery. (**A**) TEM image, (**B**) HRTEM image, and (**C**) SAED of discharge products on a-MCNTs cathodes with controlled 0.3 mAh at 50 mA g^{-1}. (**D, E**) TEM images of charged a-MCNTs cathodes at 50 mA g^{-1}.

This quasi-solid-state rechargeable Na-CO₂ battery reaction of $4Na + 3CO_2 \leftrightarrow 2Na_2CO_3 + C$ is confirmed by XRD, electron energy loss spectroscopy, and CO_2-evolution test (details can be seen in fig. S17). The morphologies of discharge products in our CPE based Na-CO₂ batteries are different from the grape-shaped products consisting of large amount of smaller particles in liquid electrolyte. As the battery discharges to 0.3 mAh at 50 mA g^{-1}, the clean a-MCNTs surface is isolatedly deposited by nanosized beans (~10 nm in diameter) (fig. S20A). The high resolution transmission electron microscopy (HRTEM) image depicts the (401) plane of Na_2CO_3 and (002) planes of carbon (JCPDS card no. 41-1487) (fig. S20B). Selected area electron diffraction shows halo rings of (-602) (201) planes of Na_2CO_3 (JCPDS card no. 86-300) (fig. S20C), indicating the existence and polycrystalline property of product Na_2CO_3. Undoubtedly, nanosized discharge products offer sufficient interfaces between products and CPE, thus benefiting product decomposition during charge. The nanosized products of Na_2CO_3 and C really disappear after charge to 0.3 mAh at 50 mA g^{-1}

(figs. S20D and E). Above results further indicate the rechargeability of the battery with reversible reaction of $4Na^+ + 3CO_2 + 4e^- \leftrightarrow 2Na_2CO_3 + C$.
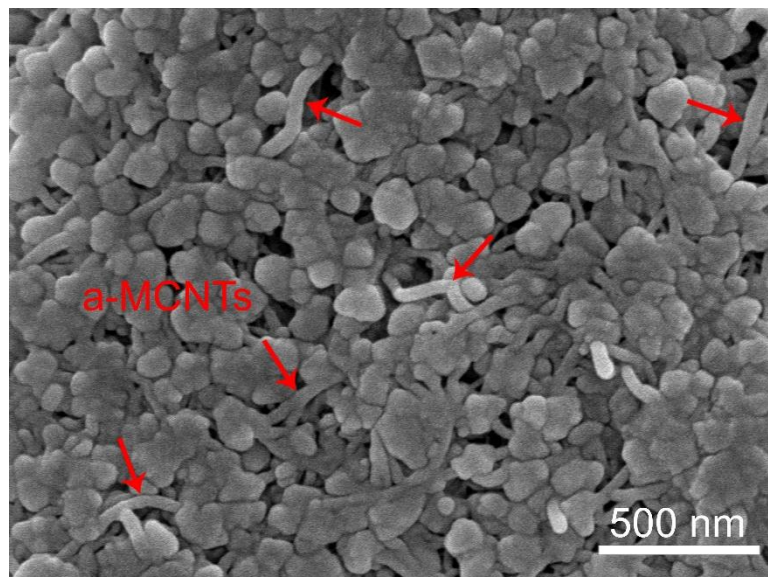

fig. S21. SEM image of a-MCNT cathode with discharge capacity of 0.1 mA·hour at 100 mA g^{-1}.

The discharged a-MCNTs cathode with capacity of 0.1 mAh is almost covered by large amount of product particles (~100 nm in diameter). The residual a-MCNTs surface is not enough to further deposite more discharge products with capacity of 0.1 mAh. In fact, the capacity of 0.3 mAh (1000 mAh g^{-1}) at 100 mA g^{-1} is obtained without fading trend (the black line in fig.4A) and the corresponding cathode is totally covered by particulate products (~100 nm in diameter, the first inset graph of fig. 4A). The product particles with larger capacity do not become bigger and we can clearly observe particles beneath superficial particles on the cathode. Therefore, the discharge products at 100 mA g^{-1} pile up rather than just growing on a-MCNTs surface.
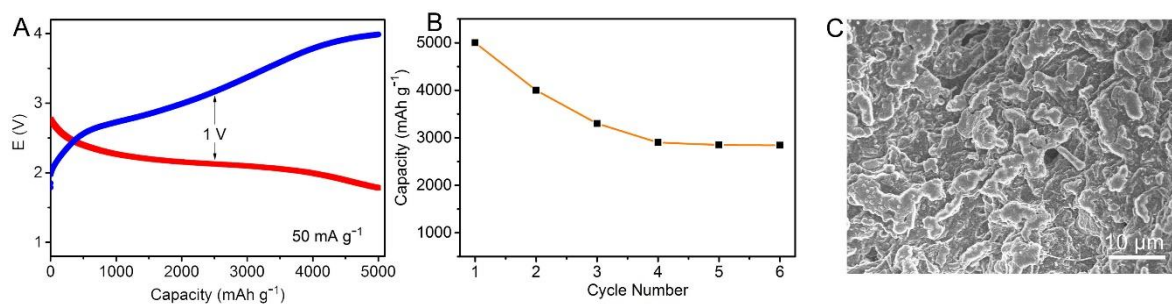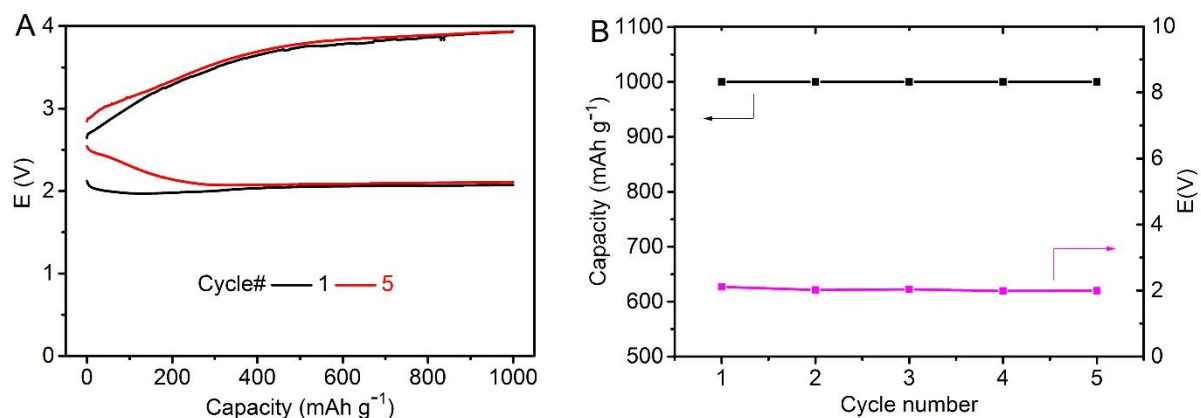
fig. S22. Full discharge and charge of quasi–solid state Na-CO$_2$ batteries. (**A**) Initial discharge/charge profiles of quasi-solid-state Na-CO$_2$ batteries with rGO-Na anodes at 50 mA g^{-1}. (**B**) Cyclability of full discharge/charge operation at 50 mA g^{-1}. (**C**) SEM image of cathode after the 6th recharge.

The capacity decay mainly results from the accumulation of residual discharge products on each charge process. At the state of large discharge capacity, higher charge overpotential is required to decompose products, which are in poor conductivity and impede the electron transfer across the electrode/products interface.
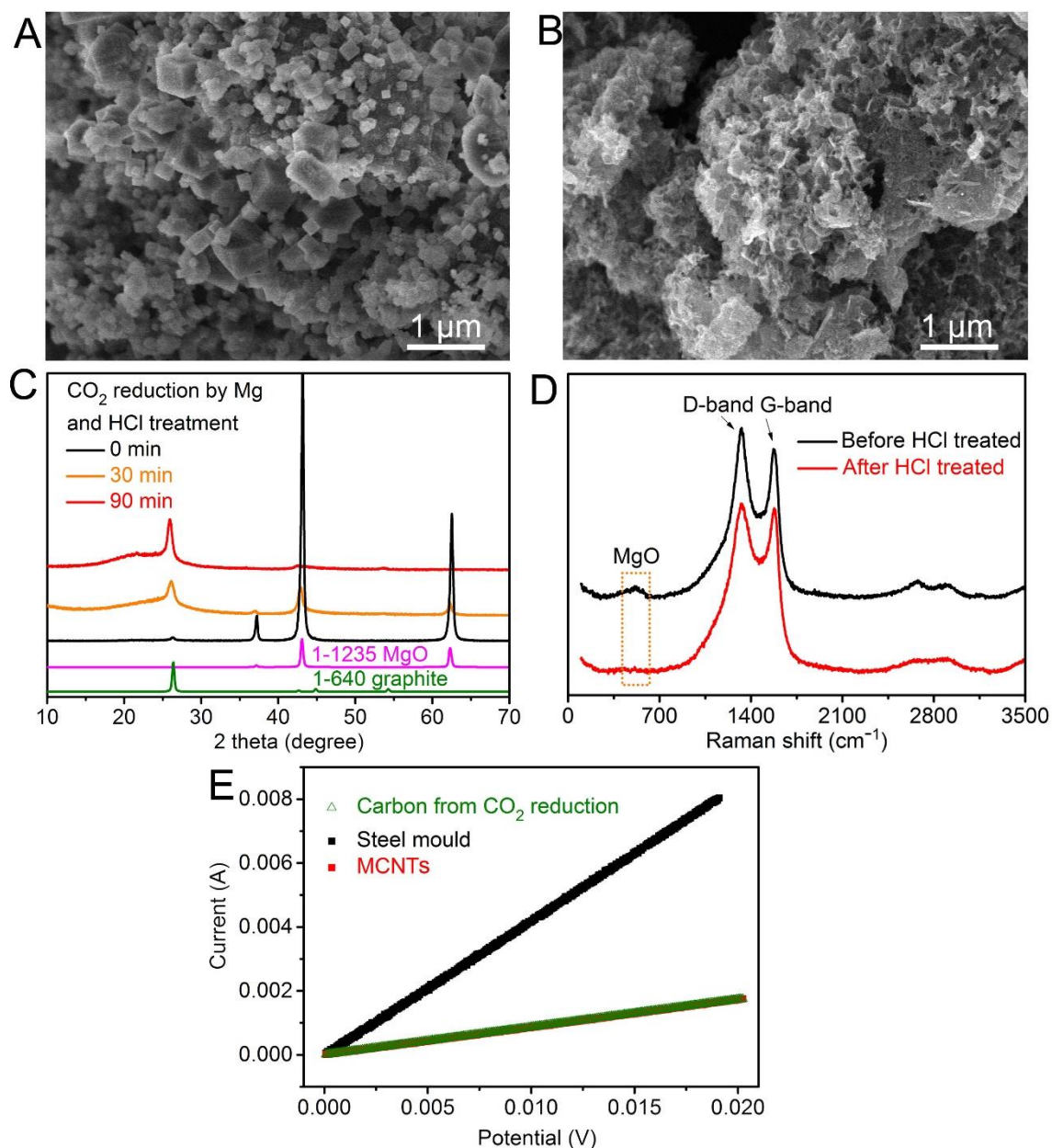
fig. S23. Characterizations of curly carbon nanosheets. (**A**) SEM images of C/MgO mixture. This mixture comes from the reaction of $2Mg + CO_2 \rightarrow 2MgO + C$. (**B**) SEM images of curly carbon nanosheets, which is obtained after C/MgO mixture is corroded in HCl solution. This new carbon is aggregated to some extent. (**C**) XRD and (**D**) Raman of C/MgO mixture and C at different states. (**E**) Electron-conductivity test of MCNTs and curly carbon nanosheets. This test is carried out in a steel mould that contains a CR2032 anode case with two stainless steel lids. During test, the mould is full of sample powders and tested in electrochemical workstation. The slope reciprocal stands for electronic resistance. Thus, the electronic resistance of MCNTs, reduced carbon, and mould is 9.17, 9.19, and 2.38 Ω, respectively.

fig. S24. Discharge/charge curves of quasi–solid state Na-CO₂ batteries with new carbon cathodes that contain curly carbon nanosheets. (**A**) Discharge/charge profiles at 200 mA g^{-1} and (**B**) Corresponding cyclability.

The new carbon possesses similar conductivity with a-MCNTs but exhibits larger overpotentials than a-MCNTs based Na-CO₂ batteries. In consideration of the merits of 3 dimentional porous cathode structure that could be offered by a-MCNTs but not the aggregated new carbon, we get to know that a-MCNTs are more suitable for Na-CO₂ batteries than our new carbon in terms of mass transfer of CO₂ and the deposition of solid products.
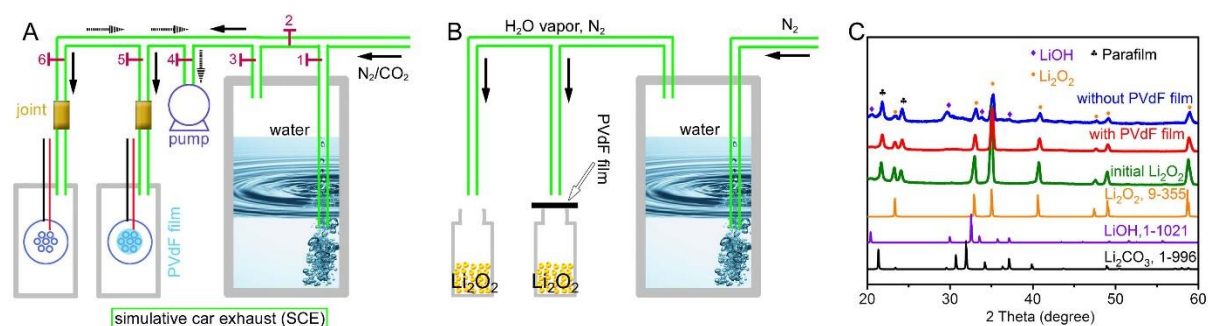

fig. S25. A device for SCE. (**A**) A device for simulative car exhaust (SCE). By using valves, we can control the ratio of CO₂/N₂ and whether it contains water or not. (**B**) A device for examining the water-resisting property of PVdF film. The blowing process goes for 10 h. (**C**) XRD patterns of Li₂O₂ powders after the examination in (B).

Ultrapure CO₂/N₂ (99.9999 %) mixture was channelled into the battery bottles through a series of valves. Firstly, 4# valve connecting the vessel and pump was opened to make sure

the elimination of initial Ar in battery vessels and air in the tubular line. Then, humid SCE gases (CO_2/N_2=1:1, 3.2 vol % H_2O) were channelled into the vessel with 1, 3, 5# valves open. The water pool can provide a saturated vapor pressure of water at 25°C. The PVdF film is hydrophobic, which can protect the battery (right) from destruction of water but permit the transmission of CO_2 and N_2. Additionally, dry SCE can be achieved by closing 1# and 3# valves and opening 2# and 6# valves.

Li_2O_2 powders are sensitive to water ($2Li_2O_2 + 2H_2O \rightarrow 4LiOH + O_2$). After blowing humid N_2 (3.2 vol % H_2O) onto the Li_2O_2 powders for 10 h (fig. S25B), the XRD patterns of Li_2O_2 powders with PVdF film protection show no visible LiOH peaks; While, XRD patterns of the bared Li_2O_2 powders present obvious LiOH peaks (fig. S25C). This result indicates that the PVdF film has good water-resisting property.
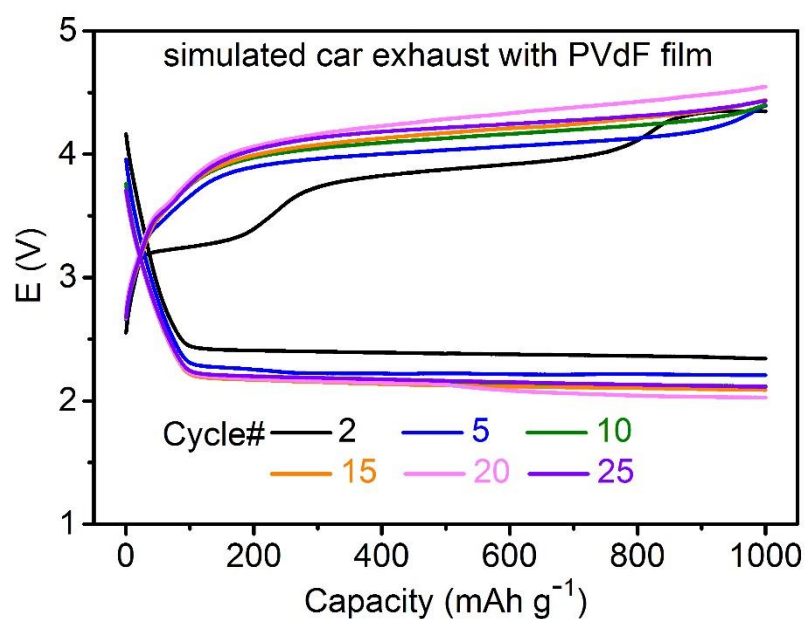
fig. S26. Discharge/charge profiles in SCE with PVDF film protection of quasi–solid state Na-CO$_2$ batteries.
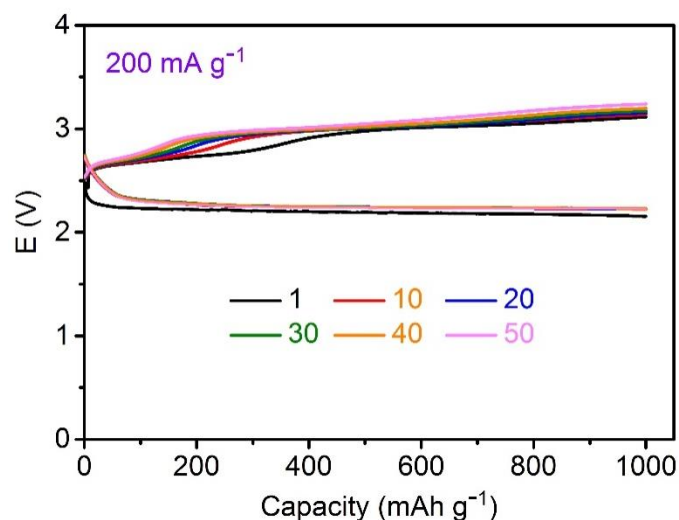
fig. S27. Discharge/charge profiles of quasi–solid state Na-CO₂ batteries at 50°C. The battery atmosphere is dry SCE with 50% CO_2 and 50% N_2 (2# condition).
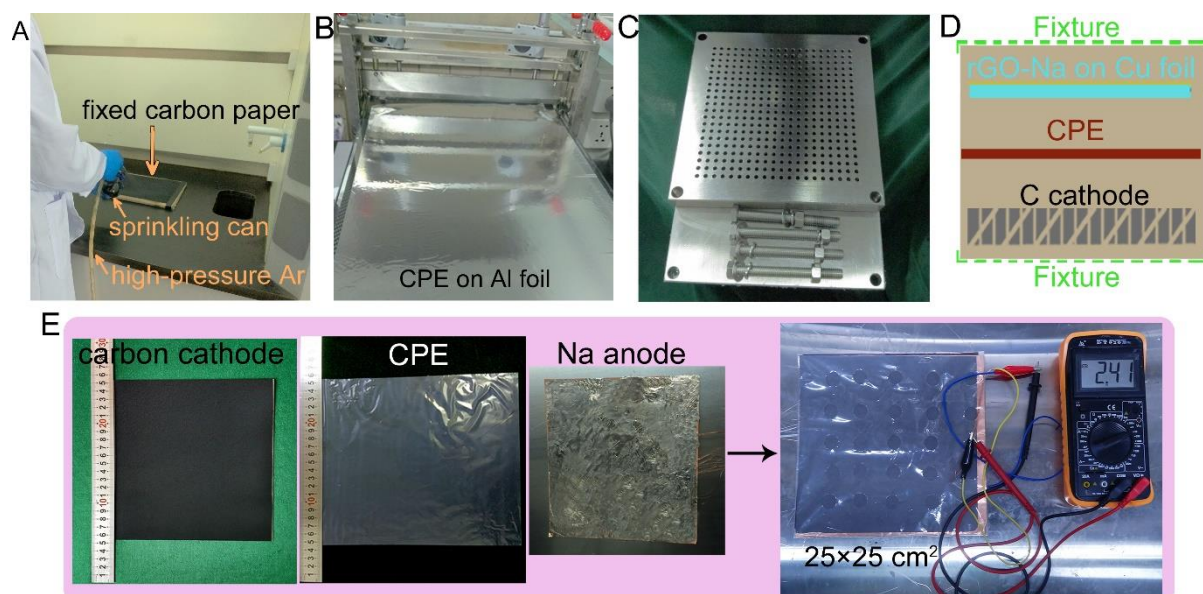
fig. S28. The preparation and assembly of large batteries. Photographs of (**A**) spraying process of carbon cathode preparation, (**B**) Casting film on a film applicator. (**C**) Photograph of two fixture plates. One plate is 304 stainless steel plate ($25 \times 25 \times 5$ cm³) with 400 holes (5 mm in diameter) and the other one is a concreate stainless steel plate ($25 \times 25 \times 2$ cm³). (**D**) A schematic diagram of the pouch-type battery. (**E**) Photographs of carbon cathode, CPE, anode, and finally assembled pouch-type battery.

During spraying process, uniform slurry containing 8 g L^{-1} of carbon particles in isopropanol is spraying on to one piece of carbon paper that is supported by a wood board. The power gas is high-pressure Ar. The obtained carbon cathode is dried in open air at room temperature. Large pieces of CPE (>20 cm × 30 cm) are casted by a film applicator and tailored to specific size prior to soaking in electrolyte.
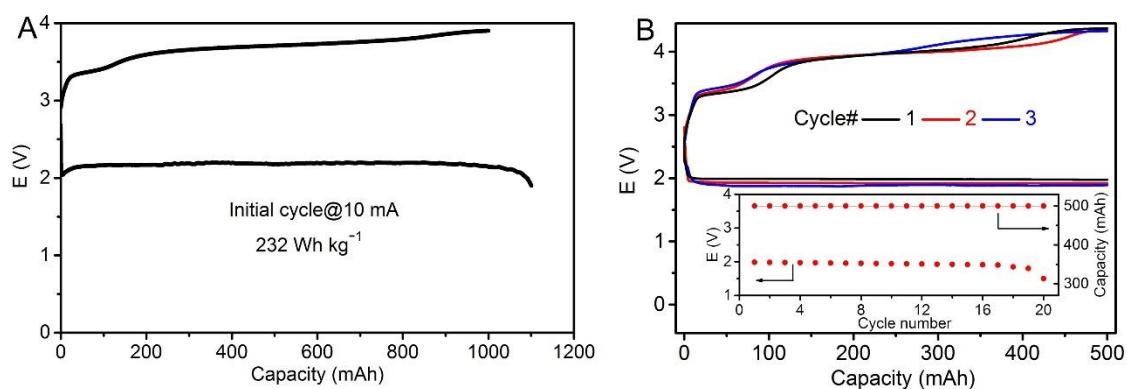
fig. S29. Pouch-type battery performance. The battery size is 20×20 cm^2. (**A**) Initial full discharge/charge profiles and (**B**) cyclability of pouch-type batteries. Rate, 10 mA.

movie S1. Sudden reaction on GO foam.

movie S2. Molten Na infusion into rGO foam.

table S1. Battery performance comparison.

Cell type	Cathode	Cut-off Capacity /Ah g^{-1}	Cyclability /cycles	Rate/ mA g^{-1}	Voltage gap /V
Li–CO$_2$	High surface area carbon (*37*)	0.75	-	-	-
Li–CO$_2$	KB (*38*)	1.00	7	30	~1.50 V
Li–CO$_2$	RGO (*39*)	1.00	20	50	1.22~1.52
Li–CO$_2$	CNT (*40*)	1.00	29	50	~1.50 V
Na–CO$_2$	Porous Carbon (*2*)	0.18	-		-
Mg–CO$_2$	Porous Carbon (*41*)	0.30	-		-
Al–CO$_2$	High surface area carbon (*37*)	0.17	-		-
Na–CO$_2$/O$_2$	Super P (*41*)	0.80	21	200	~3.00
Na–CO$_2$/O$_2$	porous carbon (*7*)	0.20	100	-	~3.50
Na–CO$_2$	t-MWCNT (*4*)	1.00	200	1000	~1.00
Quasi-solid Na–CO$_2$	a-MCNT (this work)	1.00	400	500	1.75~2.31